ISSN 1027-4510, Journal of Surface Investigation: X-ray, Synchrotron and Neutron Techniques, 2019, Vol. 13, No. 5, pp. 832–835. © Pleiades Publishing, Ltd., 2019.
Russian Text © The Author(s), 2019, published in Poverkhnost', 2019, No. 9, pp. 49–53.

Tungsten-Containing Phases in Diamond-Like Silicon–Carbon Nanocomposites

A. I. Popov[a, c, *], V. P. Afanas'ev[a], A. D. Barinov[a, c], Yu. N. Bodisko[a], A. S. Gryazev[a], I. N. Miroshnikova[a, c], M. Yu. Presnyakov[b], and M. L. Shupegin[a]

[a] *National Research University MPEI (Moscow Power Engineering Institute), Moscow, 111250 Russia*
[b] *National Research Center "Kurchatov Institute", Moscow, 123182 Russia*
[c] *Institute of Nanotechnology of Microelectronics, Russian Academy of Sciences, Moscow, 119991 Russia*
**e-mail: popovai2009@gmail.com*

Received December 17, 2018; revised January 14, 2019; accepted January 20, 2019

Abstract—Using scanning electron microscopy and X-ray photoelectron spectroscopy, we investigate the chemical forms of tungsten incorporated into diamond-like silicon–carbon films. The films are fabricated by simultaneously carrying out the plasmochemical decomposition of a silicon organic precursor and magnetron sputtering of the metal. Films of tungsten-containing diamond-like silicon–carbon nanocomposites are found to contain a considerable amount of the amorphous phase of tungsten oxide, along with nanocrystalline tungsten carbide.

Keywords: diamond-like silicon–carbon films, nanocomposites, high-resolution transmission electron microscopy, X-ray photoelectron spectroscopy

DOI: 10.1134/S1027451019050124

INTRODUCTION

Diamond-like amorphous silicon–carbon films consisting of mutually stabilizing structural carbon–hydrogen and silicon-oxide networks offer all the advantages of conventional diamond-like carbon coatings while lacking many shortcomings of the latter. This opens up new prospects for their wide use as protective coatings in space engineering [1], optoelectronics [2], and as antifriction coatings in the machine-building industry. In addition, due to high stability of the silicon–carbon matrix, the content of incorporated metal can be increased to a few tens of percent, with the matrix retaining its amorphous state. This enables us to vary the properties of nanocomposite materials based on metal-containing silicon–carbon films in broad ranges. For instance, the electrical conductivity of such materials can be changed by up to 16 orders of magnitude [4]. It is commonly accepted that the incorporation of carbide-forming metals into silicon–carbon matrices results in the formation of nanocrystals of corresponding carbides. If an incorporated metal does not produce carbides, as is the case with platinum, the nanocomposite contains nanocrystals of the metal itself. The nanocrystal sizes depend on the nature of the metal and its content and vary from 1 to 10 nm [4].

The aim of this work is to investigate the chemical forms in which metal incorporated into a diamond-like silicon–carbon matrix exists.

FABRICATION OF SAMPLES AND CHARACTERIZATION TECHNIQUES

In this work, we studied nanocomposite tungsten-containing silicon–carbon films. The films were fabricated by the plasmochemical decomposition of poly(methylphenyl)silane (PMPS; $(CH_3)_3SiO(CH_3C_6H_5SiO)_nSi(CH_3)_3$), a silicon organic precursor, with the simultaneous magnetron sputtering of tungsten onto single-crystal silicon substrates. The design of the setup enabled us to fabricate, within a single operation cycle, samples with a different tungsten content ranging from 7 to 36 at % [5]. The film thickness was around 0.5 μm. Experimental investigations—high resolution electron microscopy, electron diffraction, and energy-dispersive X-ray microanalysis—were carried out using a Titan 80–300 high-resolution scanning transmission electron microscope (STEM/TEM) and spectrometers for X-ray photoelectron spectroscopy (XPS): VersaProbe II (ULVAC-PHI) and Axis Ultra DLD (Kratos).

RESULTS OF ELECTRON MICROSCOPY AND DIFFRACTION STUDIES

Our high-resolution electron microscopy studies showed that the fabricated samples with a tungsten content in the whole range studied here represented a two-phase system consisting of nanocrystals incorporated into an amorphous silicon–carbon matrix. At a tungsten content in the range of 15–24 at %, the aver-

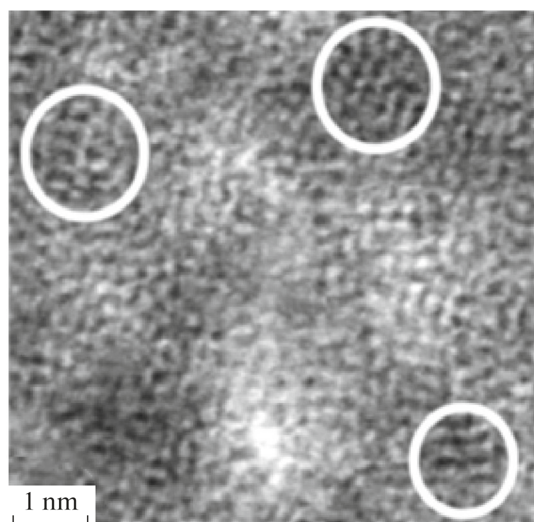

Fig. 1. Electron microscopy image of a cross section of the fabricated tungsten-containing silicon–carbon film.

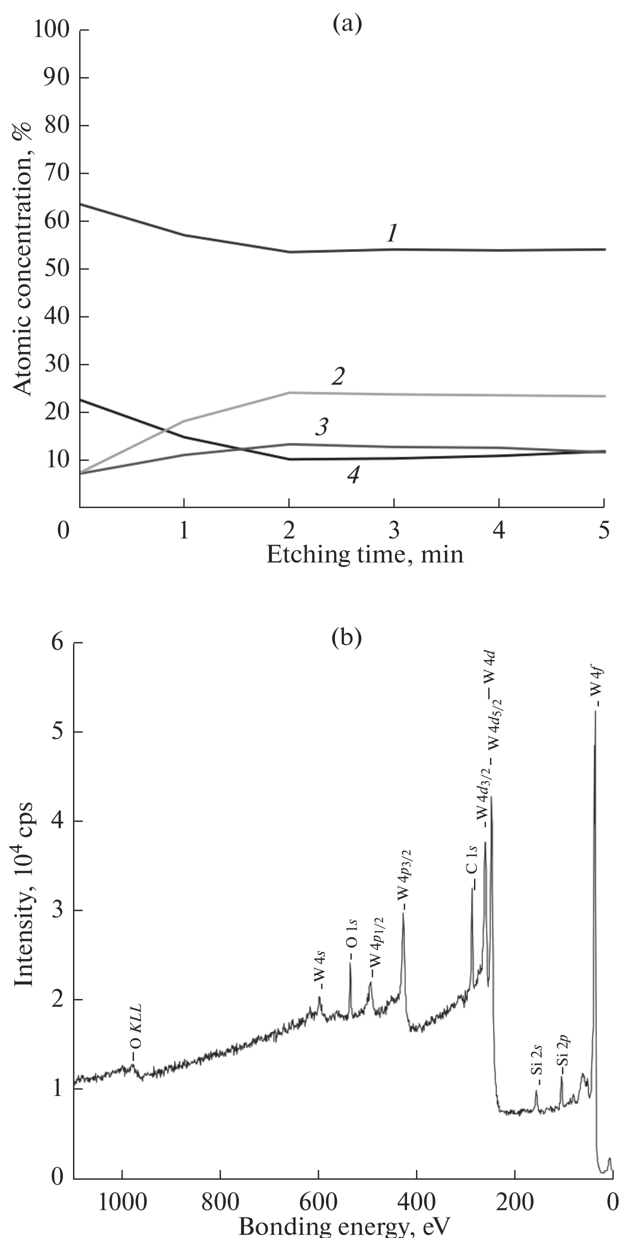

Fig. 2. (a) Element concentration profiles along the thickness of the etched layer: (*1*) C 1*s*, (*2*) W 4*f*, (*3*) Si 2*p*, and (*4*) O 1*s*. (b) Survey XPS spectrum of a sample containing 24 at % tungsten.

age nanocrystal size was 1 nm (Fig. 1). Analysis of the electron diffraction patterns identified that the crystalline inclusions were tungsten-carbide nanocrystals. However, the broadening of diffraction reflections due to the small size of the nanoparticles and the similarity between the lattice parameters of tungsten carbide (WC) and ditungsten carbide (W_2C) prevented us from identifying reliably which of these two carbides forms nanocrystals.

INVESTIGATION AND MODELING OF XPS SPECTRA

To establish the chemical composition of the tungsten-carbide nanocrystals, we carried out the XPS characterization of our samples using AlK_α monochromatic radiation. Prior to obtaining the spectrum, the surface layer was stripped off our samples by etching their surface with argon ions (ion energy, 2 keV; area, 2 × 2 mm) until a stable chemical composition was obtained (etching time, 5 min).

For a sample containing 24 at % tungsten, the element concentration profiles along the thickness of the etched layer are shown in Fig. 2a. Survey spectra were recorded at an analyzer-pass energy of $E_{\text{pass}} = 160$ eV. A survey spectrum for the sample with 24 at % tungsten that was recorded after its surface was etched is shown in Fig. 2b. High-resolution spectra in the regions of the C 1*s* peak and the W $4f_{7/2}$ and W $4f_{5/2}$ peaks were recorded at a pass energy of $E_{\text{pass}} = 40$ eV.

An XPS spectrum comprising the range of bonding energies of C 1*s* carbon atoms (280–290 eV) is shown in Fig. 3a. As can be seen, this spectrum can be fitted with two individual peaks: peak *1* at energies of 283.3–283.5 eV and peak *2* at energies of 284.3–284.5 eV. Considering that the spectrum of the precursor (i.e., PMPS) has a peak with an energy close to that of peak *2*, it is reasonable to assume that this peak corresponds to carbon atoms of the silicon–carbon matrix. At the same time, the XPS spectra of PMPS do not feature peaks with energies matching that of peak *1*. Moreover, the peak position is nearly identical to the bonding energy between carbon and tungsten atoms in tungsten carbide WC (283.2 eV) [6]. Our tungsten-containing silicon–carbon films therefore contain nanocrystals of tungsten carbide WC.

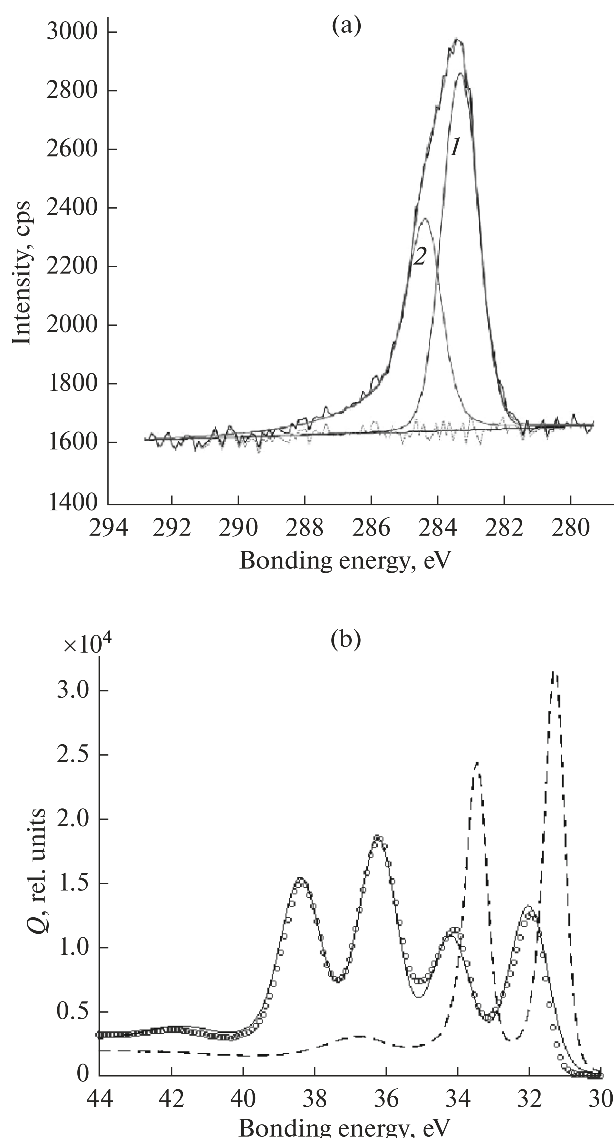

Fig. 3. Experimental (circles) and modeled (solid line) XPS spectra comprising the regions of bonding energies for (a) carbon C 1*s* (282–286 eV) and (b) tungsten W $4f_{7/2}$ and W $4f_{5/2}$ (30–44 eV) for a sample containing 28 at % W. The theoretical spectrum corresponds to a model compound containing 56% tungsten oxide and 44% tungsten carbide. The spectrum for pure tungsten [7] is shown with a dashed line.

The spectra, shown in Fig. 3, comprising regions of bonding energies of tungsten atoms (30–44 eV) also support this conclusion, because these feature peaks at 31.95 and 34.15 eV (a shift of 0.7 eV relative to peaks for pure tungsten) corresponding to tungsten–carbon chemical bonds in tungsten carbide WC [8–10]. However, the spectra under discussion feature two more very pronounced peaks: at 36.15 and 38.55 eV (a shift of 4.90 eV relative to the peaks for pure tungsten). The positions of these peaks nearly coincide with the range of bonding energies in tungsten oxide WO_3 [9, 10], suggesting that the oxide phase is present in our tungsten-containing silicon–carbon nanocomposites along with the nanocrystalline carbide phase. Since high-resolution electron microscopy and diffraction analyses revealed only the presence of metal-carbide nanocrystals in the samples, it is reasonable to assume that tungsten oxide exists in the samples in the amorphous state.

To estimate the ratio of tungsten distributed between the carbide and oxide phases, we modeled XPS spectra in the range containing bond energies of tungsten atoms in materials with different values of this ratio. For a sample containing 28 at % tungsten, the best fit to the experimental spectrum was obtained for a material in which 44% of tungsten atoms were in the carbide phase WC, while the remaining 56% formed the oxide phase WO_3 (Fig. 3b). The distribution of tungsten between the carbide and oxide phases depends on the total tungsten content in the sample. For instance, with a total tungsten content of 36 at %, the proportion of tungsten atoms forming the carbide phase increases to 55%, and, correspondingly, the proportion of tungsten forming the oxide phase falls to 45%.

We thus showed that upon the incorporation of tungsten into silicon–carbon films, this metal forms the amorphous oxide phase, along with the nanocrystalline carbide phase.

CONCLUSIONS

So far, in calculating the concentration dependences of the electrical and mechanical properties and the percolation barrier of metal-containing silicon–carbon nanocomposites, the content of the nanocrystalline carbide phase has been determined assuming that all metal atoms were in the carbide phase [11–14]. The findings of this work, however, indicate that the tungsten incorporated into the nanocrystalline silicon–carbon film is distributed approximately equally between the nanocrystalline carbide and amorphous oxide phases, which have considerably different physical properties. Therefore, the actual content of the nanocrystalline phase proved to be half of the value deemed for it, and, undoubtedly, this circumstance affected the dependences of the properties of these materials on the metal content.

Evaluating the findings of this study, we wondered if other metals when incorporated into silicon–carbon films can form oxide phases, along with carbide phases. Our analysis of published data revealed some indirect evidence of such a possibility. For instance, the electron energy loss spectrum of a tantalum-containing silicon–carbon nanocomposite, recorded near absorption edge of oxygen, featured a peak at 539 eV that is characteristic of tantalum oxide (see Fig. 15 in [14]). This question, however, requires further research. In particular, a more detailed analysis of the

XPS spectra is needed, and this, along with analysis of the peak intensities of the photoelectron lines of elements with their chemical shifts, must focus on a region containing inelastic losses of electron energy. This would enable us to find the differential cross section for the single inelastic scattering of electrons, which determines the electronic structure of the substance under study [15, 16].

FUNDING

The work was supported by the Russian Foundation for Basic Research (grant no. 19-07-00021).

REFERENCES

1. F. Mangolini, B. A. Krick, T. D. B. Jacobs, et al., Carbon **130**, 127 (2018). https://doi.org/10.1016/j.carbon.2017.12.096
2. A. I. Popov, A. D. Barinov, and M. Y. Presniakov, J. Nanoelectron. Optoelectron **9,** 787 (2014). https://doi.org/10.1166/jno.2014.1678
3. E. V. Zavedeev, O. S. Zilova, A. D. Barinov, et al., Appl. Phys. A **122,** 961 (2016). https://doi.org/10.1007/s00339-016-0508-7
4. A. Popov, *Disordered semiconductors: Physics and Applications,* 2nd ed. (Pan Stanford Publ., Stanford 2018).
5. M. L. Shupegin, Zavod. Lab. Diagn. Mater., **79** (2), 28 (2013).
6. S. T. Oyama, *The Chemistry of Transition Metal Carbides and Nitrides* (Springer, Dordrecht, 1996).
7. J. Moulder, W. Stickle, P. Sobol, and K. Bomben, *Handbook of X-Ray Photoelectron Spectroscopy* (Perkin-Elmer Corporation, Physical Electronics Division, Eden Prairie, Minnesota, 1995).
8. C. J. Powell, J. Electron Spectrosc. Relat. Phenom **185,** 1 (2012). https://doi.org/10.1016/j.elspec.2011.12.001
9. A. Katrib, F. Hemming, P. Wehrer, L. Hilaire, and G. J. Maire, J. Electron Spectrosc. Relat. Phenom **76,** 195 (1995). https://doi.org/10.1016/0368-2048(95)02451-4
10. A. V. Naumkin, A. Kraut-Vass, S. W. Gaarenstroom, and C. J. Powell, NIST X-ray Photoelectron Spectroscopy Database. Version 4.1. 2012. http://www.srdata.nist.gov/xps.
11. V. I. Polyakov, A. I. Rukovishnikiv, and P. I. Perov, Thin Solid Films **292,** 91 (1997). https://doi.org/10.1016/S0040-6090(96)08936-5
12. S. M. Rotner, V. A. Mokritskii, and V. V. Lagutin, Tekhnol. Konstr. Elektron. Appar., **6,** 58 (2006).
13. A. D. Barinov, A. I. Popov, and M. Yu. Presnyakov, Inorg Mater **53,** 690 (2017). https://doi.org/10.1134/S0020168517070019
14. M. Yu. Presnyakov, A. I. Popov, D. S. Usol'tseva, M. L. Shupegin, and A. L. Vasil'ev, Nanotechnol Russia **9,** 518 (2014). doi https://doi.org/10.1134/S1995078014050139
15. V. P. Afanas'ev, A. S. Gryazev, D. S. Efremenko, and P. S. Kaplya, Vacuum **136,** 146 (2017). https://doi.org/10.1016/j.vacuum.2016.10.021
16. V. P. Afanas'ev, G. S. Bocharov, A. V. Eletskii, O. Yu. Ridzel, P. S. Kaplya, and M. Köppen, J. Vac. Sci. Technol. **35,** 041804. https://doi.org/10.1116/1.4994788

Translated by A. Kukharuk